nature energy

ARTICLES

https://doi.org/10.1038/s41560-020-0573-1

Ultrahigh power and energy density in partially ordered lithium-ion cathode materials

Huiwen Ji[1,2,3], Jinpeng Wu[4,10], Zijian Cai[1,2,10], Jue Liu[5], Deok-Hwang Kwon[1,2], Hyunchul Kim[2], Alexander Urban[6], Joseph K. Papp[7], Emily Foley[8], Yaosen Tian[1,2], Mahalingam Balasubramanian[9], Haegyeom Kim[2], Raphaële J. Clément[8], Bryan D. McCloskey[3,7], Wanli Yang[4] and Gerbrand Ceder[1,2] ✉

The rapid market growth of rechargeable batteries requires electrode materials that combine high power and energy and are made from earth-abundant elements. Here we show that combining a partial spinel-like cation order and substantial lithium excess enables both dense and fast energy storage. Cation overstoichiometry and the resulting partial order is used to eliminate the phase transitions typical of ordered spinels and enable a larger practical capacity, while lithium excess is synergistically used with fluorine substitution to create a high lithium mobility. With this strategy, we achieved specific energies greater than 1,100 Wh kg^{-1} and discharge rates up to 20 A g^{-1}. Remarkably, the cathode materials thus obtained from inexpensive manganese present a rare case wherein an excellent rate capability coexists with a reversible oxygen redox activity. Our work shows the potential for designing cathode materials in the vast space between fully ordered and disordered compounds.

The tremendous growth of lithium-based energy storage has put new emphasis on the discovery of high-energy-density cathode materials[1]. Although state-of-the-art layered Li(Ni,Mn,Co)O_2 (NMC) cathodes achieve good power and energy density, potential further improvements in these are limited. In addition, as the Li-ion industry grows to 1 TWh of production per year, approximately one million tons of combined cobalt or nickel will be required, thereby placing significant strains on metal resources[2]. New cathodes with high energy densities made from abundant metals are crucial to sustain further Li-ion growth. Emerging materials, such as Li-rich layered oxides[3,4] and cation-disordered rock-salt-type cathodes[5,6], despite showing record-high energy densities, have yet to demonstrate a sufficient rate capability for fast rechargeable batteries, a limitation that has been attributed to a large proportion of Li_2MnO_3 in the electrode formula[4] or surface transition metal (TM) densification on O_2 loss[7,8].

When designing cathode materials, a face-centred-cubic anion framework is most beneficial for achieving dense energy storage because it is a close-packed crystalline arrangement. To obtain fast Li-transport pathways and a high power density, the cations, which include both Li and TM ions, should be optimally positioned within this anion framework. The criterion for the optimal cation arrangement was inspired by the recent discovery of the critical role of interconnecting low-energy migration channels in facilitating fast Li percolation[9]. A Li^+ ion that passes through a tetrahedral site with no face-sharing TM ions (that is, a 0-TM channel) experiences a lower electrostatic repulsion than that when it passes through a tetrahedron that face-shares with one TM ion (that is, a 1-TM channel). This mechanism is particularly important when the structure is compact. It has also been shown that a spinel-like cation order (short-range or long-range) is more efficient at creating and percolating these 0-TM channels (Fig. 1a) through the structure than other common ordering types[10]. This creates fast Li-ion networks, even in partially or fully disordered structures, and a high amount of kinetically accessible Li (Supplementary Note 1, Supplementary Fig. 1 and Supplementary Table 1).

Conventional ordered spinel cathodes have been extensively investigated. $LiMn_2O_4$ can practically only be cycled between the Mn_2O_4 and $LiMn_2O_4$ compositions[11], that is, only over half the Li content per TM of layered analogues, and therefore provides a limited energy density of about 480 Wh kg^{-1}. Ni substitution for Mn leads to a high-voltage spinel $LiNi_{0.5}Mn_{1.5}O_4$ with an improved energy density, but both spinels have limited capacities as they cannot reliably cycle over the low-voltage plateau between LiM_2O_4 and $Li_2M_2O_4$ (refs [12,13]) (M = non-Li metal ions). A spinel with excess Li, $Li_4Ti_5O_{12}$ (16.7% M sites substituted by Li) shows a desirable rate capability[14], yet the low-voltage $Ti^{3+/4+}$ couple renders it unsuitable for cathode use[15].

Here, in a departure from previous strategies, we demonstrate two bulk oxyfluorides with partial spinel-like order, $Li_{1.68}Mn_{1.6}O_{3.7}F_{0.3}$ and $Li_{1.68}Mn_{1.6}O_{3.4}F_{0.6}$ (hereafter referred to as LMOF03 and LMOF06, respectively), which achieve a high energy density, >1,100 Wh kg^{-1}, and ultrafast rate capability. Note that these compositions exhibit cation overstoichiometry compared to the ideal LiM_2O_4 stoichiometry (that is, their cation to anion ratio of 3.28:4 is larger than the 3:4 for ordered spinels) as well as Li excess because Li is partially substituted for Mn. The excess Li is used to increase the concentration of 0-TM channels for a larger capacity and better Li transport kinetics,

---

[1] Department of Materials Science and Engineering, University of California Berkeley, Berkeley, CA, USA. [2] Materials Sciences Division, Lawrence Berkeley National Laboratory, Berkeley, CA, USA. [3] Energy Storage and Distributed Resources Division, Lawrence Berkeley National Laboratory, Berkeley, CA, USA. [4] The Advanced Light Source, Lawrence Berkeley National Laboratory, Berkeley, CA, USA. [5] Neutron Scattering Division, Oak Ridge National Laboratory, Oak Ridge, TN, USA. [6] Department of Chemical Engineering, Columbia University, New York, NY, USA. [7] Department of Chemical and Biomolecular Engineering, University of California Berkeley, Berkeley, CA, USA. [8] Materials Department, University of California Santa Barbara, Santa Barbara, CA, USA. [9] X-ray Science Division, Advanced Photon Source, Argonne National Laboratory, Lemont, IL, USA. [10] These authors contributed equally: Jinpeng Wu, Zijian Cai. ✉e-mail: gceder@berkeley.edu

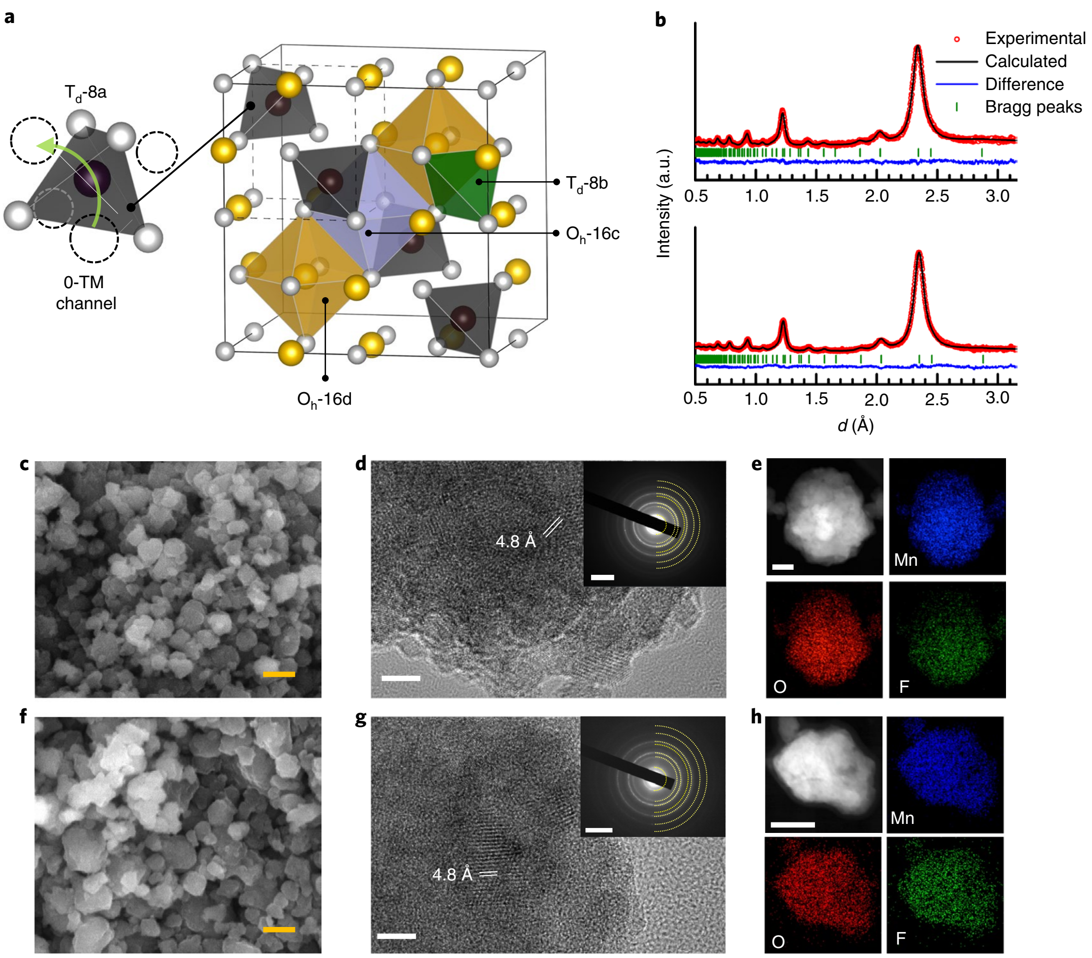

Fig. 1 | Structural and morphological characterization of two oxyfluorides LMOF03 and LMOF06. **a**, Crystal structure fragment of a perfectly ordered spinel LiM_2O_4 (M = non-Li metal ions), with the high-symmetry Wyckoff positions T_d-8a, T_d-8b, O_h-16c, O_h-16d highlighted as coloured polyhedra. A pseudo face-centered-cubic anion framework is outlined with black dashed lines. The black, yellow and silver spheres represent the occupying Li, M and F/O atoms, respectively. Inset: the enlarged T_d-8a site illustrates a 0-TM channel, in which none of its four face-sharing octahedral sites (dashed circles) is occupied by a TM. **b**, Rietveld refinement using time-of-flight neutron diffraction data ($2\theta = 67°$) at room temperature for LMOF03 (top) and LMOF06 (bottom). **c**,**f**, SEM images of as-synthesized LMOF03 (**c**) and LMOF06 (**f**). Scale bars, 200 nm. **d**,**g**, High-resolution transmission electron microscopy images of LMOF03 (**d**) and LMOF06 (**g**). Scale bars, 5 nm. Insets: electron diffraction patterns. Scale bars, $5\,nm^{-1}$. The selected area electron diffraction patterns can be indexed to a spinel lattice, with the *d* spacings determined to be 4.8, 2.5, 2.1, 1.6, 1.5, 1.2 and 1.0 Å. **e**,**h**, EDS mapping of Mn, O and F in LMOF03 (**e**) and LMOF06 (**h**). Scale bars, 50 nm.

whereas the tunability in F substitution allows for lower valences of Mn and an improved cyclability[16]. Importantly, the unconventionally high Li-excess and fluorination levels are achieved through mutual facilitation: the excessive amount of Li is charge-balanced by F substitution, whereas the concentrated fluorination is only feasible because of the presence of the Li-rich local environments[17]. Finally, we used the cation overstoichiometry to induce partial M (dis)order so that the voltage step and first-order transition, characteristic of fully ordered spinels discharged past the LiM_2O_4 composition, are removed. Remarkably, we found that half of the observed capacity in LMOF03 comes from reversible oxygen (O) redox, suggesting that the participation of anionic redox is not an intrinsic limitation to rate capability. Our results show the tremendous potential of designing high-performance and resource-efficient cathode materials in the large space between fully ordered compounds and random solid solutions.

Oxyfluorides with partial spinel-like order

LMOF03 and LMOF06 are synthesized through mechanochemical alloying. Elemental analysis shows their chemical compositions to be nearly identical to those of the targeted ones (Supplementary Table 2). We found that the overstoichiometric Li is critical in stabilizing the high fluorination levels against phase segregation into LiF and Mn_2O_3 during synthesis. Structural refinements using combined synchrotron X-ray and neutron diffraction data confirmed that both compounds adopt a spinel-like structure (space group: $Fd\bar{3}m$), with a pseudo face-centred-cubic anion framework (outlined by dashed lines in Fig. 1a). The site occupancies of Mn were obtained by refining X-ray diffraction patterns (Supplementary Fig. 2), which were then taken as a starting model to fit the time-of-flight neutron data. Figure 1b shows the final neutron refinement, which indicates a good agreement between the observed and calculated peak positions and intensities (refinement details in Supplementary Tables 3–5 and Supplementary Figs. 3 and 4). The refined lattice parameter is 8.1161(16) Å for LMOF03 and 8.1458(14) Å for LMOF06. In an ordered stoichiometric spinel, the tetrahedral 8a and octahedral 16d sites are fully occupied by Li and M, respectively, leaving the 8b and 16c sites vacant. In the two spinel-like oxyfluorides, however, complete cation order is not observed: (1) Mn is distributed between the 16c and 16d sites, with 14–16% of the total

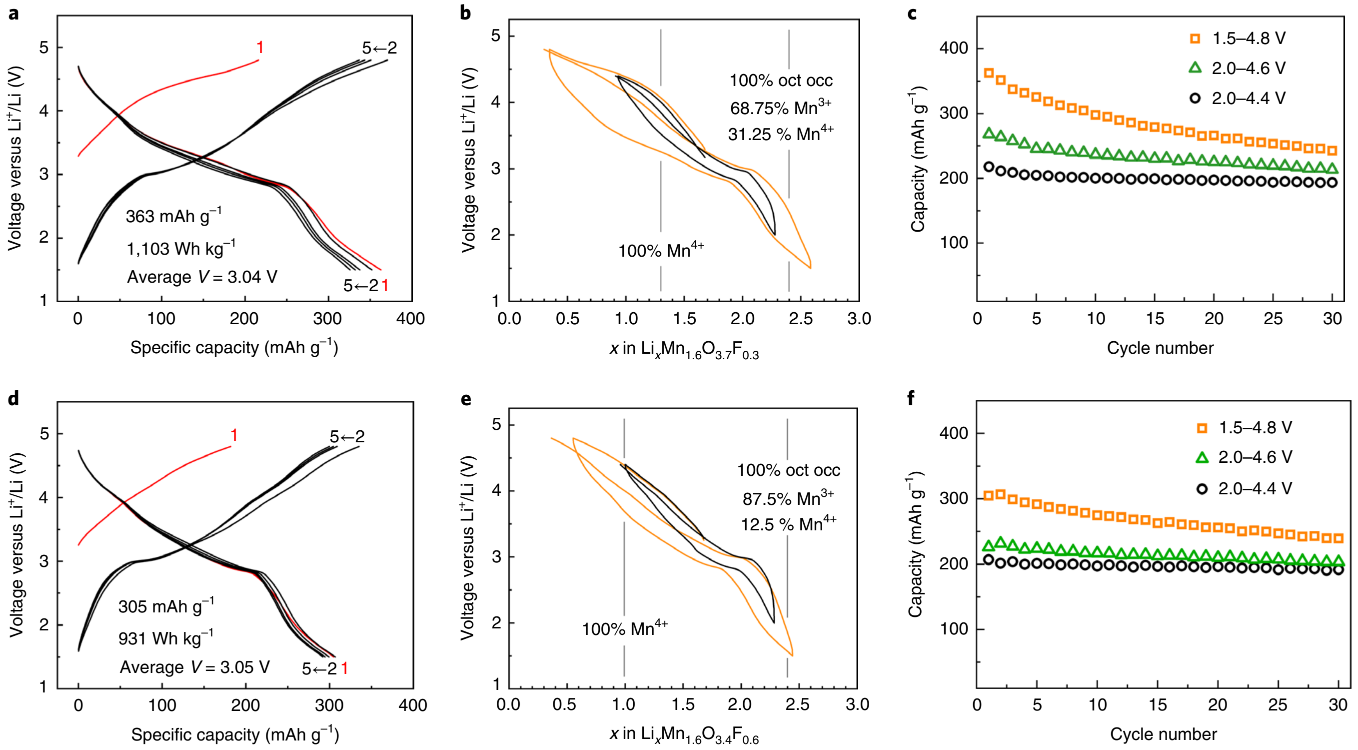

Fig. 2 | Galvanostatic charge and discharge performance of LMOF03 and LMOF06 at 50 mA g^{-1} at room temperature. a,**d**, Voltage profiles, started in charge, for the first five cycles obtained over the 1.5–4.8 V range for LMOF03 (**a**) and LMOF06 (**d**). **b**,**e**, Voltage profiles during the first cycle and the second charge over voltage windows of 2.0–4.4 V (black) and 1.5–4.8 V (orange) for LMOF03 (**b**) and LMOF06 (**e**). **c**,**f**, Capacity retention over various voltage windows for LMOF03 (**c**) and LMOF06 (**f**). oct occ, octahedral occupancy.

Mn content occupying 16c sites, and (2) only half of the 8a sites are occupied by Li. The remaining Li content is distributed between the 16c and 16d sites, with LMOF06 containing more Li in the 16c site than LMOF03. If we define a structure to be perfectly spinel-ordered (0% disorder) when all Mn is in the octahedral 16 site, or to be completely disordered (100% disorder) when Mn equally occupies the 16c and 16d sites, then the degree of disorder derived from the above structural refinement is 32.5% for LMOF03 and 27.5% for LMOF06.

The primary particle size is estimated using scanning electron microscopy (SEM) to be 100–200 nm for LMOF03 and 100–300 nm for LMOF06, as shown in Fig. 1c,f. The agglomeration of primary particles into secondary particles was also observed (Supplementary Fig. 5). The nanoscale crystalline lattice and elemental distribution are characterized using high-resolution transmission electron microscopy and energy-dispersive spectroscopy (EDS). The results are shown in Fig. 1d,e,g,h. For both materials, the size of the crystallite domains within the polycrystalline primary particles is estimated to be 10 nm. A characteristic *d* spacing of ~4.8 Å for the spinel (111) faces is highlighted with white lines on crystallite grains that are properly orientated (Fig. 1d,g). Both materials show electron diffraction patterns that can be indexed based on a spinel crystal structure. ^{7}Li and ^{19}F solid-state NMR spectroscopy suggests the bulk integration of Li and F into the spinel structure (Supplementary Figs. 6 and 7 and Supplementary Notes 2 and 3). Although LMOF06 might contain some diamagnetic impurities (Supplementary Note 2), the amount is unlikely to be significant because EDS elemental mapping across the particles reveals a uniform distribution of Mn, O and F (Fig. 1e,h).

Large capacity beyond expected TM contribution

Both spinel-like-ordered oxyfluorides demonstrate remarkable gravimetric capacity and energy density, as shown in Fig. 2a,d. The theoretical Li capacity for both compounds is 2.4 Li per formula unit (f.u.) assuming that all the octahedral vacancies can be occupied, but with no face-sharing octahedral and tetrahedral occupancy (that is, limiting compositions of $Mn_{1.6}O_{4-x}F_x$ and $Li_{2.4}Mn_{1.6}O_{4-x}F_x$ on charge and discharge, respectively), which corresponds to 389 and 387 mA h g^{-1} for LMOF03 and LMOF06, respectively. In the limiting Li composition of $Li_{2.4}Mn_{1.6}O_{4-x}F_x$, Mn is not expected to be fully reduced to Mn^{3+}, which makes the theoretical Mn capacity based on the Mn$^{3+/4+}$ redox couple 1.1 Li per f.u. (178 mA h g^{-1}) for LMOF03 and 1.4 Li per f.u. (226 mA h g^{-1}) for LMOF06. The Li-site-controlled discharge limit and the Mn^{4+} charge limit are marked in Fig. 2b,e by vertical lines.

A capacity larger than the theoretical Mn redox capacity was observed for both compounds. When cycled at 50 mA g^{-1} over the range 1.5–4.8 V, LMOF03 delivered a reversible capacity of 363 mAh g^{-1} (a specific energy of 1,103 Wh kg^{-1}), which corresponds to 2.25 Li per f.u., among the highest capacities reported to date for a Li-ion cathode[5,6,18]. Even if the discharge was limited to 2 V (or 3 V), the capacity and specific energy were still as high as 309 mAh g^{-1} and 1,010 Wh kg^{-1} (or 202 mAh g^{-1} and 726 Wh kg^{-1}), respectively. Approximately half of the observed capacity in the 1.5–4.8 V range (~0.95 Li per f.u.) was obtained at Li contents below $x = 1.3$, when all the Mn^{3+} is expected to be oxidized to Mn^{4+} (Fig. 2b), which suggests the participation of a major charge compensation mechanism, possibly from oxygen, aside from the Mn redox. This extra capacity was accompanied by an increased voltage hysteresis. The maximum value of this hysteresis during the first cycle occurred near $x \approx 1.0$ and was approximately 0.91 V, which is comparable to that observed in heavily fluorinated disordered rock salts, for example, $Li_2Mn_{2/3}Nb_{1/3}O_2F$ in 1.5–5 V and Li_2MnO_2F in 2–4.8 V (refs [5,19]), but much smaller than that in Li-rich oxides, for example, disordered rock salt $Li_{1.3}Mn_{0.4}Nb_{0.3}O_2$ (~1.45 V hysteresis in 1.5–4.8 V) (ref. [6])

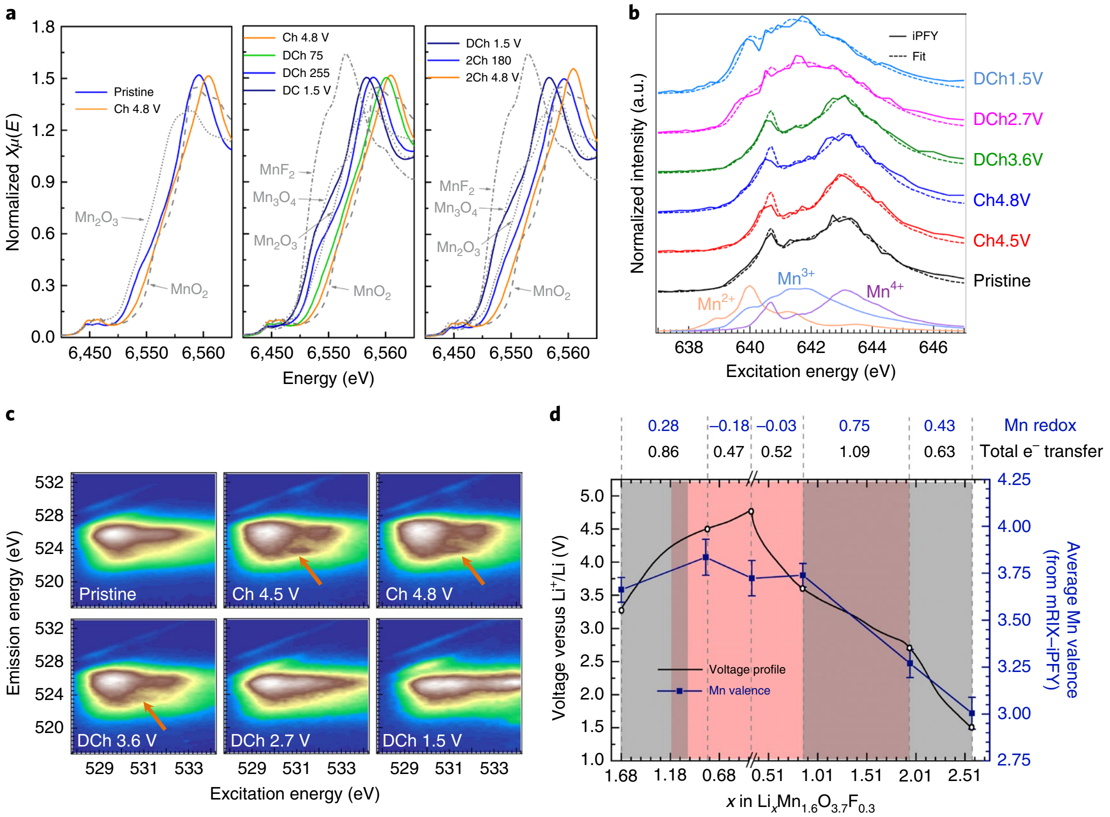

Fig. 3 | Redox mechanism of LMOF03. **a**, Operando Mn *K*-edge XANES spectra during the first charge (left)–discharge (centre) cycle and second charge (right). The selected states are labelled by voltage or capacity. **b**, Ex-situ Mn L_3-edge iPFY spectra extracted from Mn-L_3 mRIXS at six states of charge and discharge during the first cycle. Standard spectra of MnO, Mn_2O_3 and MnO_2 are included as references. **c**, Ex situ O *K*-edge mRIXS collected during the initial charge–discharge cycle. **d**, Quantification of Mn redox reactions during the initial cycle. The Mn valences were obtained from a linear fit of the Mn-L_3 mRIXS–iPFY data at the six electrochemical states. Each error bar represents the standard error calculated by combining the standard errors of the $Mn^{2+}/Mn^{3+}/Mn^{4+}$ fractions, which were obtained via linear fitting each Mn-L_3 mRIXS–iPFY spectrum. The numbers of total charge transfer and electron transfer from Mn redox per f.u. over different voltage ranges are denoted in black and blue, respectively, above the panel. Ch, first charge; DCh, first discharge; 2Ch, second charge.

and layered $Li_{1.2}Ni_{0.13}Mn_{0.54}Co_{0.13}O_2$ (~1.23 V hysteresis in 2.0–4.8 V) (ref. [3]). Such voltage hysteresis is commonly observed in Li-rich layered and disordered rock-salt cathode materials that involve O redox and is likely associated with the different reaction paths between the charge and discharge processes, but the precise origin of it is not yet established. When narrowing the voltage window, hysteresis reduces and capacity retention improves. LMOF03 exhibited a slightly lower first-cycle gravimetric capacity (and energy) of 268 mAh g^{-1} (868 Wh kg^{-1}) when cycled between 2.0 and 4.6 V, and 218 mAh g^{-1} (690 Wh kg^{-1}) when cycled between 2.0 and 4.4 V. The doubled F content in LMOF06 increases the theoretical TM capacity to ~1.4 Li per f.u., which results in an improved cyclability and negligible concomitant oxygen loss (Supplementary Figs. 8–10). After 30 cycles, nearly 80% of the initial capacity was retained over the range 1.5–4.8 V, and ~93% is retained over the range 2.0–4.4 V. The voltage hysteresis is also noticeably smaller than that for LMOF03, when comparing data collected over similar voltage windows.

The chemical and structural complexity of the spinel-like-ordered oxyfluorides results in tunable voltage profiles. The two compounds show sloping voltage curves which provide easy monitoring of the state of charge. The curves are different from the wide plateaus commonly observed in $LiMn_2O_4$ or $LiNi_{0.5}Mn_{1.5}O_4$[12], which suggests the suppression of two-phase reactions and Li-vacancy ordering. The observed capacity near 4 V is considerably lower than that in $LiMn_2O_4$ due to the reduced Li occupancy in 8a sites. As a result of the Li overstoichiometry and partial cation (dis)order, a low number of Li$^+$ in tetrahedral sites is energetically favoured as it minimizes the interaction of Li$^+$ with metal ions in adjacent face-sharing 16c sites. Consequently, more Li is active at a lower voltage of ~3 V, which is associated with the occupation of octahedral sites. The voltage profile of LMOF06 is steeper than that of LMOF03, which results in a slightly lower capacity of 305 mAh g^{-1} (931 Wh kg^{-1}) over the range 1.5–4.8 V. Given that the additional $Mn^{3+/4+}$ capacity in LMOF06 is unlikely to cause this difference, plausible origins include a greater diversity of Li local environments and more F-bonded Li$^+$ ions with a higher site energy, induced by the larger F content in LMOF06. This speculation about the Li-site distribution is also corroborated by the ^{7}Li NMR data, as the ^{7}Li pj-MATPASS (projected magic-angle turning and phase-adjusted sideband separation) spectrum obtained for LMOF06 is slightly broader than that obtained for LMOF03 (Supplementary Fig. 6).

TM and anionic redox mechanisms

To investigate the charge transfer mechanism that accompanies Li extraction and insertion, operando X-ray absorption near-edge structure (XANES) in the hard X-ray region and ex situ mapping of resonant inelastic X-ray scattering (mRIXS) measurements in the soft X-ray region were performed.

The overall Mn redox behaviour in LMOF03 was revealed by the Mn *K*-edge XANES spectra, as shown in Fig. 3a at selected states of charge. The material showed a reversible Mn redox process, with no detectable Mn oxidation beyond 4+. In the initial charge,

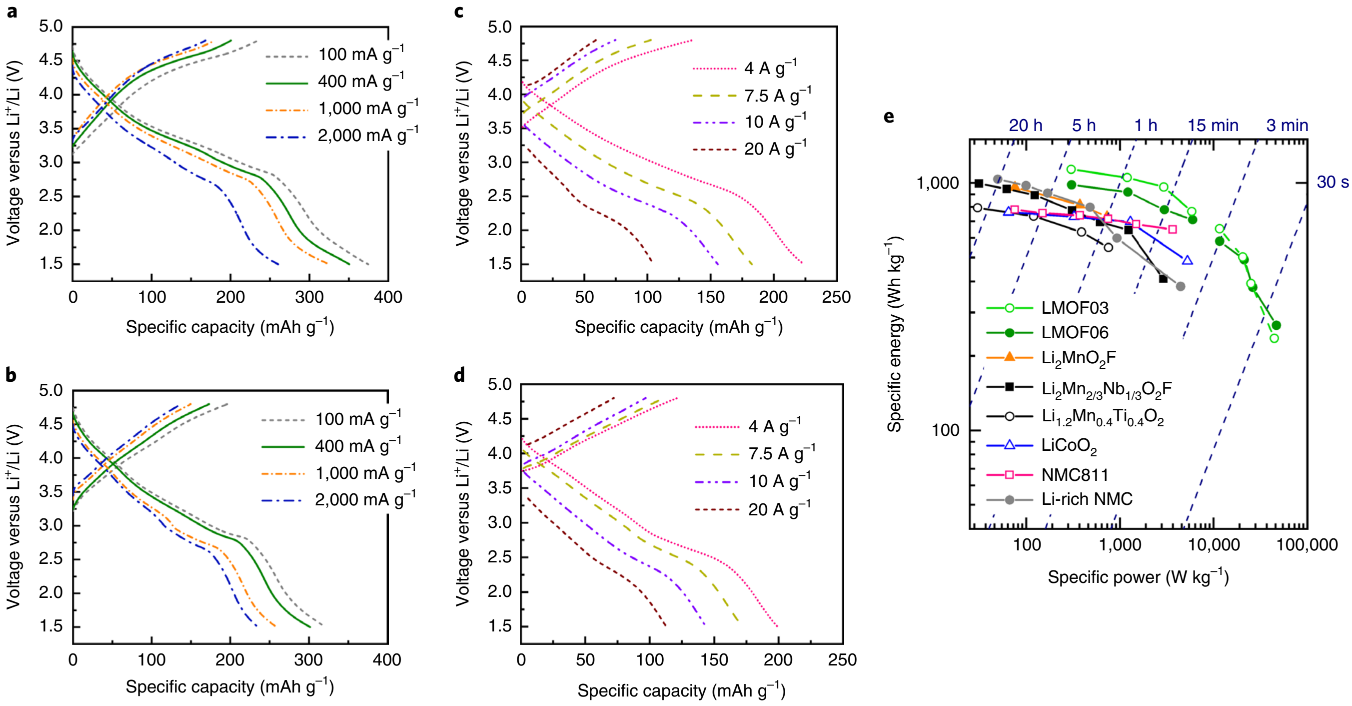

Fig. 4 | Rate capability measurements. a–d, Galvanostatic voltage profiles of LMOF03 (**a**,**c**) and LMOF06 (**b**,**d**) at lower (**a**,**b**) and higher (**c**,**d**) rates. A fresh cell was used for each rate test. **e**, Ragone plot comparing the specific energy and power of LMOF03 and LMOF06 to those of state-of-the-art Li-ion cathodes with optimized rate performance as reported in the literature[5,19,32,35–37]. The loading density of the cathode film was 2–3 mg cm^{-2}. The weight ratio of the active material, carbon black and Teflon in cathode films was 7:2:1 for rates from 100 to 2,000 mA g^{-1}, and 4:5:1 for rates from 4 to 20 A g^{-1}. The testing parameters for the cited materials are summarized in Supplementary Table 8.

the Mn *K*-edge shifted slightly to an energy close to that in MnO_2 (Mn^{4+} reference), consistent with the expected contribution from the $Mn^{3+/4+}$ redox capacity in this region. On discharge to 1.5 V, the edge position reversed towards an energy between Mn_2O_3 (Mn^{3+} reference) and Mn_3O_4 (mixed Mn^{2+}/Mn^{3+}), followed by a reversible oxidation to Mn^{4+} again during the second charge. A similar mechanism was observed for LMOF06 (Supplementary Fig. 11), except that the pristine Mn state was less oxidized (Supplementary Fig. 15 and Supplementary Table 7) due to the higher F content in the as-prepared material. Note that the main edges of the XANES spectra correspond to the excitations of core electrons to Mn 4*p* states rather than the 3*d* valence states, and therefore cannot be used to precisely quantify the Mn oxidation states[20].

To accurately quantify the Mn redox contribution as a function of the state of charge, we employed Mn *L*-edge mRIXS on LMOF03 and extracted the inverse partial fluorescence yield (iPFY) signal through a state-of-the-art high-efficiency mRIXS system[21,22] (see technical details on the data analysis in Supplementary Fig. 12). The extracted mRIXS–iPFY spectra at six electrochemical states are displayed in Fig. 3b (solid curves). The overall line shape changed slightly during the initial charge, which indicates a limited Mn oxidation, but underwent an obvious evolution during the subsequent discharge, which, when compared with the reference spectra, indicates a significant reduction of Mn. The observation is consistent with the trend of the XANES results discussed above. As demonstrated in multiple previous cases, the Mn *L*-edge spectral line shape is sensitive to the Mn oxidation states and can be quantitatively fitted by a linear combination of $Mn^{2+/3+/4+}$ reference spectra[22–24]. The fitting results presented in Fig. 3b (dashed curves) agree with the experimental data (fitting details in Supplementary Table 6). The Mn valence change and the amount of electron transfer due to the Mn redox reactions thus obtained are plotted in Fig. 3d. The mRIXS–iPFY quantification of the Mn valence reveals that Mn redox reactions mostly happen below 4.5 V on charge and between 3.6 and 1.5 V on discharge (grey shaded areas in Fig. 3d). Above 4.5 V on charge, the Mn oxidation state slightly dropped and remained largely unchanged until 3.6 V discharged, which indicates that the electrochemical capacity in this region (red shaded area) is entirely contributed by a non-Mn redox process.

A mismatch between the cationic redox contribution and the electrochemical capacity often indicates O redox reactions. We thus employed a systematic study of O-*K* mRIXS. The technique reliably detects the oxidation of lattice O by measuring the characteristic feature at an emission energy of around 523.7 eV and an excitation energy of 531.0 eV (refs [22,25,26]) (orange arrows in Fig. 3c), which originates from an excitation to unoccupied/oxidized O 2*p* orbitals[26]. This characteristic signal emerged at 4.5 V and grew stronger in intensity on the charge to 4.8 V, and reversibly weakened during discharge until 2.7 V. The reversible evolution of the mRIXS feature on cycling provides direct experimental evidence for a reversible lattice O redox process in our electrode system.

The combined Mn-*L* and O-*K* mRIXS results consistently reveal the Mn and O redox mechanism: the contribution of Mn redox reactions to electrochemical capacity (grey shading in Fig. 3d) is limited during the initial charge, but becomes more dominant during discharge below 3.6 V. However, O oxidation (red shading in Fig. 3d) dominates the charge process, followed by reversible lattice O reduction until 2.7 V. Note that the mRIXS observation of the extended anionic redox activity towards low voltages during discharge is found in many other Li-ion and Na-ion electrodes[22,27]. In addition, the slight drop in Mn valence state when charged from 4.5 V to 4.8 V strongly indicates the impact of the TM-O coupling nature on O oxidation processes, a phenomenon noted previously[28,29].

During the second charge, as shown in Supplementary Figs. 13 and 14 and Supplementary Table 6, the observed capacity initially

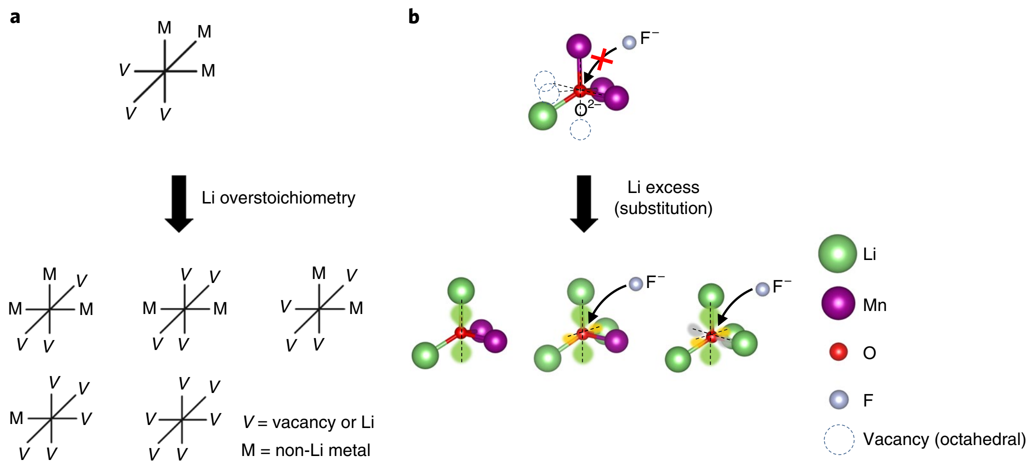

Fig. 5 | Illustration of partially (dis)ordered cation and anion local environments in a spinel-like structure that arise from Li overstoichiometry and substitution. a, Diverse M configurations in an octahedral geometry around anions. M-richer cation arrangements are not shown given their low occurrence in the presence of overstoichiometric Li. **b**, Change in the local bonding environment of anions from a stoichiometric spinel to a Li-excess spinel. The dumbbell-shaped clouds in green, yellow and grey schematically represent the unhybridized O 2*p* orbitals.

originated from Mn oxidation when the voltage was below 2.95 V. It then showed a mixed contribution from both Mn and O oxidation until 4.0 V, above which the Mn oxidation state remained nearly constant to leave O oxidation as the only source for electron extraction. After the subsequent discharge, the Mn valence reversibly decreased to a value close to that observed after the first full cycle.

The reversible redox reactions are consistent with a reversible lattice change during cycling, as shown in the ex situ X-ray diffraction patterns (Supplementary Fig. 16). The data reveal a similar trend for LMOF03 and LMOF06, with the second-cycle charge process restoring the same delithiated lattice as after the first charge. Ex situ synchrotron diffraction data (Supplementary Note 4 and Supplementary Figs. 17 and 18) confirmed the preservation of a spinel structure during cycling. The extent of Mn disorder in the 16d and 16c octahedral sites as obtained by Rietveld refinement remained constant on charge and only increased when discharged below 2.7 V, which was then reversed during the subsequent charge process.

Ultrahigh rate capability despite O redox

An ultrahigh rate capability was observed in LMOF03 and LMOF06, as shown in Fig. 4a–d. All the rate capability tests were carried out using galvanostatic charge and discharge at the specified rate without holding the voltage at the top of charge. At the extremely high rates from 4 to 20 A g^{-1}, to remove all other possible rate limitations, we diluted the electrode and increased its electron conductivity by using a high carbon loading. Similar high rate capability was demonstrated before in high-carbon-content electrodes for a different material[30]. Although this shows the intrinsic rate capability of the cathode material, in commercial electrodes the carbon loading would have to be reduced through carbon coating to more efficiently form a conductive network, as has been demonstrated for $LiFePO_4$ (ref. [31]).

At 100 mA g^{-1}, LMOF03 delivers a gravimetric capacity of over 370 mAh g^{-1}. When cycled 20 times faster at 2,000 mA g^{-1}, the observed capacity is reduced only moderately by ~30% to 260 mAh g^{-1} and the discharge process takes about eight minutes. As the theoretical Mn capacity is only 178 mAh g^{-1} in LMOF03, a significant portion of the observed capacity at 2,000 mA g^{-1} is still expected to originate from reversible O redox. The fact that such large capacities are able to sustain high rates of charge and discharge despite a major contribution from O redox is in contrast to previous observations of sluggish kinetics in O-redox-involved Li-rich layered oxide cathodes[32,33] or cation-disordered rock salts[5,6]. Our observation suggests that O redox is not intrinsically slow. Instead, it is possible that the specific local environments that stabilize oxidized O species are sluggish in their formation in other compounds, for example, because their formation may involve slow M migration. M migration is often observed at high voltages accompanying O redox in Li-rich layered cathodes[34]. In contrast, in our materials, no significant increase in M disorder was observed even at the top of charge (Supplementary Figs. 17 and 18). Hence, it is possible that the ultrafast kinetics in LMOF03, even with major O redox contributions, is due to the lack of M migration. However, further investigation is required to provide a detailed mechanism. LMOF06 exhibited an even higher rate capability than that of LMOF03, with a less pronounced polarization growth as the rate increased from 100 mA g^{-1} to 20 A g^{-1}.

The rate performance of the two spinel-like oxyfluorides is compared to that of state-of-the-art Li-ion cathodes in a Ragone plot shown in Fig. 4e. Only the best rate capability reported in literature, achieved through nano-sizing, surface coating or discharge after slow charging or voltage-holding, is included[5,19,32,35–37] (details in Supplementary Table 8). When compared to cathodes that involve O redox as part of their charge compensation mechanism, for example, $Li_{1.2}Mn_{0.4}Ti_{0.4}O_2$, $Li_2Mn_{2/3}Nb_{1/3}O_2F$ and the Li-rich (Ni,Mn,Co) oxide (Li-rich NMC), the specific power of LMOF03 and LMOF06 at any given energy density is at least one order of magnitude higher, resulting in the delivery of, for example, 900 Wh kg^{-1} of energy, within minutes rather than hours. Even when compared to the state-of-the-art $LiNi_{0.8}Mn_{0.1}Co_{0.1}O_2$ cathode (NMC811), at the highest literature-reported specific power ~3,000 W kg^{-1}, both LMOF03 and LMOF06 are still superior in terms of specific energy.

The importance of cation overstoichiometry and Li excess

Fully ordered structures are discrete endpoints of the extensive configurational space of partially (dis)ordered materials. Relaxing the requirement for long-range order in cathode materials enables one to access new degrees of freedom to design their electrochemical properties but requires a precise understanding of the role that each chemical and structural variable plays in the materials performance.

The two partially ordered oxyfluoride spinels shown in this article are representatives of our strategy to use partial cation order to simultaneously tune multiple chemical and structural factors, as shown in the illustration in Fig. 5. We chose to start from a spinel endpoint with the knowledge that a spinel-type cation short-range order creates a robust percolation of low-barrier Li migration channels that persists even at a fairly low Li-to-M ratio[10]. The cation overstoichiometry and partial order introduces extra Li and creates partial occupancy on 16c sites, while reducing the occupancy on 8a and 16d sites, and thereby creates a state that is in between an ordered spinel and a disordered rock salt. This state of partial order enables several compositional and structural modifications that are beneficial to performance.

The cation (or Li) overstoichiometry facilitates a partial M (dis)order by reducing the tetrahedral occupancy and thus relaxing the constraint that M ions must order in a facial configuration on all octahedral cation clusters. It leads to the diverse cation arrangements shown in Fig. 5a. This partial M (dis)order removes the collective 8a-to-16c Li migration, which in ordered spinels is responsible for a first-order phase transition and a large voltage step when they are lithiated past the LiM_2O_4 composition. As Fig. 2 shows, in the partially ordered LMOF03 and LMOF06, the voltage profiles show no discernible steps or phase transitions, which leads to a more facile charge and discharge.

A key factor in the high rate capability is probably the cation overstoichiometry and the resulting partial M (dis)order. Additional cations cannot be inserted into a stoichiometric spinel during an electrochemical process without creating face-sharing polyhedra of tetrahedral and octahedral cations. Although M–Li or M–M face sharing is highly unlikely due to their strong electrostatic repulsion, Li–Li face sharing may be possible, at least in metastable configurations. Very high Li mobility in anodes[38] and solid state electrolytes[39] has recently been linked to such Li–Li face sharing as it creates configurational frustration and high-energy Li states that are beneficial to Li mobility.

Besides enhancing transport and percolation, Li excess (that is, Li substitution) also activates O redox and enables partial F substitution for O. F substitution is important to lower the Mn valence and in other materials has been shown to reduce or remove O loss even when anion redox is present[5]. The manner by which Li excess enables anion redox and fluorination in these materials can be understood from the local anion bonding environment, as illustrated in Fig. 5b. In a conventional stoichiometric spinel $LiMn_2O_4$, each anion is covalently bonded to three Mn ions. When Li excess is introduced, the number of Li-rich local environments increases, and thereby enables easier fluorination with fewer high-energy Mn–F bonds for each F^- ion introduced[17]. The increased number of ionic O–Li bonds also leads to the appearance of high-lying unhybridized O 2*p* orbitals that act as reservoir of additional oxidizable electrons[40].

In summary, two design guidelines were followed in this work. First, Li overstoichiometry, that is, shifting the composition from $LiMn_2O_4$ to $Li_{1.28}Mn_2O_4$, was utilized to induce partial Mn disorder, and thereby eliminate the first-order transition and obtain a smooth and continuous voltage profile without discrete steps. Second, Li excess, that is, shifting the composition further from $Li_{1.28}Mn_2O_4$ to $Li_{1.68}Mn_{1.6}(O,F)_4$, was introduced to increase the kinetically accessible Li capacity and to enable fluorination and reversible O redox with more Li-rich environments. The two cathode materials thus obtained, LMOF03 and LMOF06, exhibit capacities and rate capabilities among the highest reported to date. Our simple yet effective design strategy opens up a vast chemical space in the search for new cathodes with both high energy and high power, and made from earth-abundant metals. Future improvements are expected in these materials through the partial replacement of Mn^{4+} by high-valence non-redox-active d^{10} or d^0 ions (for example, Sb^{5+}, Nb^{5+} and Mo^{6+}) and through the exploration of different or mixed redox-active TM species (for example, Ni^{2+}, V^{3+} and Cr^{3+}), as well as through the fine-tuning of the fluorination level to allow for an optimized balance between TM and O redox. The insight gained about partial structural order tuning in relation to electrochemical performance is also applicable to the materials design of Li-ion anodes as well as the optimization of conductivity in solid-state electrolytes for beyond Li-ion technologies.

Conclusions

We have demonstrated that combining a kinetically-advantageous partial-spinel-like cation order with substantial Li excess and F substitution is effective for achieving both a high energy density and an excellent rate capability in Li-ion battery cathodes. Following these design strategies, a high specific energy >1,100 Wh kg^{-1} (and capacity >360 mA h g^{-1}) was obtained for LMOF03, with nearly half of the capacity coming from O redox processes, a phenomenon that has been intensely studied in Li-rich layered Ni–Mn–Co oxides and disordered rock-salts, but is uncommon in spinel-type cathodes. A significant proportion of the capacity is retained at high cycling rates. Furthermore, we showed that the two chemical handles for structural tuning, namely, cation overstoichiometry and Li excess, can be strategically optimized to allow for fast Li transport kinetics, optimized voltage profiles and a largely tunable F-doping level and thus TM capacity to achieve the desired cyclability. Our discovery provides a model for the realization of both fast and dense energy storage in Li-ion cathode materials.

Methods

Synthesis. LMOF03 and LMOF06 were synthesized by mixing stoichiometric Li_2MnO_3 (obtained by firing Li_2CO_3 (Alfa Aesar, 99.0%) and MnO_2 (Alfa Aesar, 99.9%) at 800 °C in air for 16 h), MnF_2 (Alfa Aesar, 99%), Mn_2O_3 (Sigma-Aldrich, 99%) and MnO_2 using a Retsch PM200 planetary ball mill. A precursor powder of batch size 1 g, along with five 10-mm (diameter) and ten 5-mm (diameter) stainless-steel balls, was dispensed into a 50 ml stainless-steel jar, which was then sealed with safety closure clamps in an argon-filled glove box. We monitored the purity of the products by performing ex situ X-ray diffraction after every 5 or 10 h of mechanochemical ball milling and adjusted the synthesis time accordingly. After high-energy ball milling at 450 r.p.m. for 25 and 21 h for LMOF03 and LMOF06, respectively, the phase-pure product was obtained mechanochemically. The two target materials can also be obtained using a different set of precursors, including Li_2O, Mn_2O_3, MnO_2 and LiF. Note that we present LMOF06 as the composition with the highest fluorination in the article because this is the limit at which we are confident about the solubility of F. Above this level, impurities LiF and Mn_2O_3 as determined by XRD show up. We also synthesized $LiMn_2O_4$ as a baseline material by ball milling a stoichiometric mixture of Li_2MnO_3, Mn_2O_3 and MnO_2, under the same conditions as for LMOF03 and LMOF06. After 12 h of milling, an X-ray diffraction pattern indexed to a phase-pure $LiMn_2O_4$ without impurity peaks was obtained (Supplementary Fig. 19a and Supplementary Note 5).

Electrochemistry. The fabrication of cathode electrodes was done in an argon-filled glove box. The active material (70 wt%) was first manually mixed with Super C65 carbon black (Timcal, 20 wt%) in a mortar for 45 min. After adding polytetrafluoroethylene (Dupont, 10 wt%) as a binder, the mixture was rolled into a thin film to be used as a cathode. The loading density of the cathode film was ~5 mg cm^{-2}. Coin cells (CR2032) were assembled by using 1 M $LiPF_6$ in ethylene carbonate and dimethyl carbonate solution (volumetric 1:1, Sigma-Aldrich, battery grade) as the electrolyte, glass microfibre filters (Whatman) as separators and Li metal foil (FMC) as the anode. The sealed coin cells were then tested on an Arbin battery cycler at room temperature. For rate capability tests at high current densities from 4 to 20 A g^{-1}, the weight ratio of the active material, carbon black and binder in the cathode films was 4:5:1. The loading density of the cathode film for all rate capability tests was 2–3 mg cm^{-2}.

Compositional, structural and morphological characterization. Elemental analysis was performed by Luvak Inc. using direct-current plasma emission spectroscopy (ASTM E 1097-12) for the metal species and an ion-selective electrode method (ASTM D1179-16) for fluorine. Ex situ synchrotron diffractions of both pristine and cycled powder were taken at the Advanced Photon Source in Argonne National Laboratory on Beamline 11-ID-B ($\lambda = 0.2113$ Å). The cycled powder was prepared by mixing pristine material with carbon (in a 9:1 weight ratio), cycling the loose powder mixture at 5 mA g^{-1}, followed by equilibrating at the designated voltage until the current was below 0.2 mA g^{-1}. The obtained powder was then washed with dimethyl carbonate and dried in vacuum. Neutron powder diffraction experiments were carried out at the Spallation Neutron Source in Oak Ridge National Laboratory on the Nanoscale Ordered Materials Diffractometer[41]. The samples for neutron diffraction were synthesized using the ^{7}Li-enriched precursor $^{7}Li_2MnO_3$, which was obtained by calcinating stoichiometric $^{7}Li_2CO_3$ and MnO_2 at 800 °C in air for 16 h. All the synchrotron and neutron data were analysed using the TOPAS software package[42] Scanning transmission electron microscopy, electron diffraction patterns and EDS mapping were acquired at the Molecular Foundry in Lawrence Berkeley National Laboratory on a JEM-2010F microscope equipped with an X-Mas EDS detector. SEM images were also obtained at the Molecular Foundry on a Zeiss Gemini Ultra 55 analytical field-emission scanning electron microscope.

Operando Mn K-edge X-ray absorption spectroscopy. For the operando XANES experiments, modified coin cells were used with holes in the centre of all the stainless-steel parts and sealed with X-ray transparent Kapton tapes. A galvanostatic scan rate of 30 mA g^{-1} was used. The measurement was conducted in transmission mode at room temperature using Beamline 20-BM at the Advanced Photon Source of Argonne National Laboratory. The incident energy was selected using a Si(111) monochromator and the beam intensity was reduced by 15% using a Rh-coated mirror to minimize high-order harmonics. Reference spectra of the Mn metal were collected simultaneously using a pure Mn foil. The resultant XANES data were analysed using the Athena software package. The energies of the spectra were calibrated using the first inflection points from the reference Mn spectrum.

mRIXS. mRIXS was measured at the iRIXS endstation on Beamline 8.0.1 of the Advanced Light Source in Lawrence Berkeley National Laboratory[21]. The mapping data were collected using an ultrahigh efficiency modular spectrometer[43] with an excitation energy step of 0.2 eV. The resolution of the excitation energy was 0.35 eV and that of the emission energy was 0.25 eV. The final two-dimensional maps were obtained via multistep data processing as elaborated in a previous study[44]. The intensity of the mRIXS is represented by a colour scale (in Fig. 3c and Supplementary Fig. 12a).

Mn-L_3 iPFY. Mn-L_3 iPFY was achieved through the formula iPFY = a/PFY_O, where a is a normalization coefficient and PFY_O is the integrated fluorescence intensity over the O K emission energy range (490–530 eV, white dashed box in Supplementary Fig. 12a) from the Mn-L_3 mRIXS. In contrast to the distorted total fluorescence yield obtained from conventional Mn-L_3 soft X-ray absorption spectroscopy (shown as a yellow solid spectrum in Supplementary Fig. 12b), the non-distorted Mn-L_3 iPFY spectra can be quantitatively fitted using a linear combination of the standard spectra of $Mn^{2+/3+/4+}$, as demonstrated and detailed before[23].

Solid-state NMR. ^{19}F and ^{7}Li NMR data were collected on both LMOF03 and LMOF06 powders using a Bruker Avance 300 MHz (7.05 T) wide-bore NMR spectrometer with Larmor frequencies of 282.40 and 116.64 MHz, respectively, at room temperature. The data were obtained using 60 kHz magic-angle spinning with a 1.3 mm double-resonance probe. ^{19}F and ^{7}Li NMR data were referenced to LiF ($\delta(^{19}F) = -204$ ppm and $\delta(^{7}Li) = -1$ ppm). Line-shape analysis was carried out within the Bruker Topspin software using the SOLA line-shape simulation package.

^{7}Li spin echo spectra were acquired on all samples using a 90° radiofrequency (RF) pulse of 0.6 μs and a 180° RF pulse of 1.2 μs at 200 W. A recycle delay of 30 s was used for LiF, whereas a recycle delay of 50 ms was used for LMOF03 and LMOF06. ^{7}Li pj-MATPASS[45] isotropic spectra were also acquired on the LMOF03 and LMOF06 samples using a 90° RF pulse of 0.6 μs at 200 W with a recycle delay of 50 ms.

The resonant frequency range of the ^{19}F nuclei in the LMOF03 and LMOF06 samples was larger than the excitation bandwidth of the RF pulse used in the NMR experiment. To obtain the full spectrum, nine spin echo spectra were collected for each sample in frequency steps of 280 ppm or 79 kHz from −1,120 to 1,120 ppm, where the step size was slightly less than the excitation bandwidth of the RF pulse. The individual subspectra were processed using a zero-order phase correction and then added to give an overall sum spectrum in the absorption mode that required no further phase correction. This method, termed 'spin echo mapping'[46], 'frequency stepping'[47,48] or 'VOCS' (variable offset cumulative spectrum)[49], is able to uniformly excite the broad F signals by providing a large excitation bandwidth. Individual ^{19}F spin echo spectra were collected using a 90° RF pulse of 2.9 μs and a 180° RF pulse of 5.8 μs at 154.8 W with a recycle delay of 50 ms. For reference, a spin echo spectrum was collected for LiF using similar RF pulses, but with a recycle delay of 30 s. A ^{19}F background spectrum obtained on the empty probe using the same conditions as for the LMOF03 and LMOF06 samples showed no significant background signal.

Differential electrochemical mass spectrometer measurement. Gas-evolution measurements were collected using a differential electrochemical mass spectrometer system as described in previous publications[16,50]. Electrochemical cells of a modified Swagelok design were prepared in a glove box with thin film cathodes composed of active materials (70 wt%), Super C65 carbon black (Timcal, 20 wt%) and polytetrafluoroethylene (Dupont, 10 wt%) and a loading density of ~7 mg cm^{-2} (based on active materials). The electrolyte, separators, and anodes used were identical to those used for the coin cell tests in this study. Differential electrochemical mass spectrometer cells were cycled with a current density of 20 mA g^{-1} under a static head of argon pressure (~0.2 bar) at room temperature.

Li-percolation simulations. Percolating Li diffusion pathways through 0-TM channels were computed using the Monte Carlo method of Urban et al.[10] as implemented in the Dribble software (https://github.com/urban-group/dribble). All the simulations employed cubic cells with 3,456 $Li_xTM_yO_2$ formula units (6,912 cation sites) that are commensurate with the layered (α-$NaCoO_2$), spinel ($Li_2Mn_2O_4$), γ-$LiFeO_2$ and rock-salt crystal structures. Each simulation was repeated 500 times. Percolation of the 0-TM diffusion pathways and kinetically accessible 0-TM capacities in the ideal cation orderings of spinel and the layered structure were determined by decorating all the cation sites with TM ions at the beginning of the simulation, followed by substituting Li for TM on a randomly selected site of the Li sublattice at each Monte Carlo step. Once the Li sublattice was fully decorated with Li ions, the Li substitution was continued for the sites of the TM sublattice. Cation mixing was modelled by interchanging a fraction of the sites on the Li and TM sublattices at the beginning of the simulation. Interchanging 50% of the sites resulted in equivalence of the two sublattices and corresponds to the fully disordered rock-salt structure (that is, the degree of cation mixing is 100%). More details are given by Urban et al. in ref. [10].

Data availability

The datasets generated and analysed during the current study are available from the corresponding author upon reasonable request.

Received: 8 August 2019; Accepted: 4 February 2020;

References

1. Xu, B., Qian, D., Wang, Z. & Meng, Y. S. Recent progress in cathode materials research for advanced lithium ion batteries. *Mat. Sci. Eng. R* **73**, 51–65 (2012).
2. Olivetti, E. A., Ceder, G., Gaustad, G. G. & Fu, X. Lithium-ion battery supply chain considerations: analysis of potential bottlenecks in critical metals. *Joule* **1**, 229–243 (2017).
3. Thackeray, M. M. et al. Li_2MnO_3-stabilized $LiMO_2$ (M = Mn, Ni, Co) electrodes for lithium-ion batteries. *J. Mater. Chem.* **17**, 3112–3125 (2007).
4. Yu, X. et al. Understanding the rate capability of high-energy-density Li-rich layered $Li_{1.2}Ni_{0.15}Co_{0.1}Mn_{0.55}O_2$ cathode materials. *Adv. Energy Mater.* **4**, 1300950 (2014).
5. Lee, J. et al. Reversible Mn^{2+}/Mn^{4+} double redox in lithium-excess cathode materials. *Nature* **556**, 185–190 (2018).
6. Yabuuchi, N. et al. High-capacity electrode materials for rechargeable lithium batteries: Li_3NbO_4-based system with cation-disordered rocksalt structure. *Proc. Natl Acad. Sci. USA* **112**, 7650–7655 (2015).
7. Lee, J. et al. A new class of high capacity cation-disordered oxides for rechargeable lithium batteries: Li–Ni–Ti–Mo oxides. *Energy Environ. Sci.* **8**, 3255–3265 (2015).
8. Armstrong, A. R. et al. Demonstrating oxygen loss and associated structural reorganization in the lithium battery cathode $Li[Ni_{0.2}Li_{0.2}Mn_{0.6}]O_2$. *J. Am. Chem. Soc.* **128**, 8694–8698 (2006).
9. Lee, J. et al. Unlocking the potential of cation-disordered oxides for rechargeable lithium batteries. *Science* **343**, 519–522 (2014).
10. Urban, A., Lee, J. & Ceder, G. The configurational space of rocksalt-type oxides for high-capacity lithium battery electrodes. *Adv. Energy Mater.* **4**, 1400478 (2014).
11. Gummow, R., de Kock, A. & Thackeray, M. Improved capacity retention in rechargeable 4 V lithium/lithium-manganese oxide (spinel) cells. *Solid State Ion.* **69**, 59–67 (1994).
12. Manthiram, A., Chemelewski, K. & Lee, E.-S. A perspective on the high-voltage $LiMn_{1.5}Ni_{0.5}O_4$ spinel cathode for lithium-ion batteries. *Energy Environ. Sci.* **7**, 1339–1350 (2014).
13. Lee, E.-S., Nam, K.-W., Hu, E. & Manthiram, A. Influence of cation ordering and lattice distortion on the charge–discharge behavior of $LiMn_{1.5}Ni_{0.5}O_4$ spinel between 5.0 and 2.0 V. *Chem. Mater.* **24**, 3610–3620 (2012).
14. Feckl, J. M. et al. Nanoscale porous framework of lithium titanate for ultrafast lithium insertion. *Angew. Chem. Int. Ed.* **51**, 7459–7463 (2012).
15. Ferg, E., Gummow, R., De Kock, A. & Thackeray, M. Spinel anodes for lithium-ion batteries. *J. Electrochem. Soc.* **141**, L147–L150 (1994).
16. Lee, J. et al. Mitigating oxygen loss to improve the cycling performance of high capacity cation-disordered cathode materials. *Nat. Commun.* **8**, 981 (2017).
17. Richards, W. D., Dacek, S. T., Kitchaev, D. A. & Ceder, G. Fluorination of lithium-excess transition metal oxide cathode materials. *Adv. Energy Mater.* **8**, 1701533 (2018).
18. Zuo, Y. et al. A high-capacity O_2-type Li-rich cathode material with a single-layer Li_2MnO_3 superstructure. *Adv. Mater.* **30**, 1707255 (2018).
19. House, R. A. et al. Lithium manganese oxyfluoride as a new cathode material exhibiting oxygen redox. *Energy Environ. Sci.* **11**, 926–932 (2018).

20. Manceau, A., Marcus, M. A. & Grangeon, S. Determination of Mn valence states in mixed-valent manganates by XANES spectroscopy. *Am. Mineral.* **97**, 816–827 (2012).
21. Qiao, R. et al. High-efficiency in situ resonant inelastic X-ray scattering (iRIXS) endstation at the Advanced Light Source. *Rev. Sci. Instrum.* **88**, 033106 (2017).
22. Dai, K. et al. High reversibility of lattice oxygen redox quantified by direct bulk probes of both anionic and cationic redox reactions. *Joule* **3**, 518–541 (2019).
23. Li, Q. et al. Quantitative probe of the transition metal redox in battery electrodes through soft X-ray absorption spectroscopy. *J. Phys. D* **49**, 413003 (2016).
24. Qiao, R. et al. Revealing and suppressing surface Mn(II) formation of $Na_{0.44}MnO_2$ electrodes for Na-ion batteries. *Nano Energy* **16**, 186–195 (2015).
25. Yang, W. & Devereaux, T. P. Anionic and cationic redox and interfaces in batteries: advances from soft X-ray absorption spectroscopy to resonant inelastic scattering. *J. Power Sources* **389**, 188–197 (2018).
26. Zhuo, Z. et al. Spectroscopic signature of oxidized oxygen states in peroxides. *J. Phys. Chem. Lett.* **9**, 6378–6384 (2018).
27. Gent, W. E. et al. Coupling between oxygen redox and cation migration explains unusual electrochemistry in lithium-rich layered oxides. *Nat. Commun.* **8**, 2091 (2017).
28. Sathiya, M. et al. Reversible anionic redox chemistry in high-capacity layered-oxide electrodes. *Nat. Mater.* **12**, 827–835 (2013).
29. Luo, K. et al. Anion redox chemistry in the cobalt free 3*d* transition metal oxide intercalation electrode $Li[Li_{0.2}Ni_{0.2}Mn_{0.6}]O_2$. *J. Am. Chem. Soc.* **138**, 11211–11218 (2016).
30. Kang, B. & Ceder, G. Battery materials for ultrafast charging and discharging. *Nature* **458**, 190–193 (2009).
31. Dominko, R. et al. Impact of the carbon coating thickness on the electrochemical performance of $LiFePO_4$/C composites. *J. Electrochem. Soc.* **152**, A607–A610 (2005).
32. Martha, S. K., Nanda, J., Veith, G. M. & Dudney, N. J. Electrochemical and rate performance study of high-voltage lithium-rich composition: $Li_{1.2}Mn_{0.525}Ni_{0.175}Co_{0.1}O_2$. *J. Power Sources* **199**, 220–226 (2012).
33. Konishi, H., Gunji, A., Feng, X. & Furutsuki, S. Effect of transition metal composition on electrochemical performance of nickel–manganese-based lithium-rich layer-structured cathode materials in lithium-ion batteries. *J. Solid State Chem.* **249**, 80–86 (2017).
34. Hong, J. et al. Metal–oxygen decoordination stabilizes anion redox in Li-rich oxides. *Nat. Mater.* **18**, 256–265 (2019).
35. Teranishi, T. et al. High-rate capabilities of ferroelectric $BaTiO_3$–$LiCoO_2$ composites with optimized $BaTiO_3$ loading for Li-ion batteries. *ECS Electrochem. Lett.* **4**, A137–A140 (2015).
36. Ji, H. et al. Hidden structural and chemical order controls lithium transport in cation-disordered oxides for rechargeable batteries. *Nat. Commun.* **10**, 592 (2019).
37. Noh, H.-J., Youn, S., Yoon, C. S. & Sun, Y.-K. Comparison of the structural and electrochemical properties of layered $Li[Ni_xCo_yMn_z]O_2$ ($x=1/3$, 0.5, 0.6, 0.7, 0.8 and 0.85) cathode material for lithium-ion batteries. *J. Power Sources* **233**, 121–130 (2013).
38. Schmidt, W. et al. Small change—great effect: steep increase of Li ion dynamics in $Li_4Ti_5O_{12}$ at the early stages of chemical Li insertion. *Chem. Mater.* **27**, 1740–1750 (2015).
39. Kozinsky, B. et al. Effects of sublattice symmetry and frustration on ionic transport in garnet solid electrolytes. *Phys. Rev. Lett.* **116**, 055901 (2016).
40. Seo, D.-H. et al. The structural and chemical origin of the oxygen redox activity in layered and cation-disordered Li-excess cathode materials. *Nat. Chem.* **8**, 692–697 (2016).
41. Neuefeind, J. et al. The nanoscale ordered materials diffractometer NOMAD at the spallation neutron source SNS. *Nucl. Instrum. Meth. Phys. Res. B* **287**, 68–75 (2012).
42. Coelho, A. A. TOPAS and TOPAS-Academic: an optimization program integrating computer algebra and crystallographic objects written in C++. *J. Appl. Crystallogr.* **51**, 210–218 (2018).
43. Chuang, Y.-D. et al. Modular soft X-ray spectrometer for applications in energy sciences and quantum materials. *Rev. Sci. Instrum.* **88**, 013110 (2017).
44. Wu, J. et al. Elemental-sensitive detection of the chemistry in batteries through soft -ray absorption spectroscopy and resonant inelastic -ray scattering. *J. Vis. Exp.* **134**, e57415 (2018).
45. Hung, I. et al. Isotropic high field NMR spectra of Li-ion battery materials with anisotropy >1 MHz. *J. Am. Chem. Soc.* **134**, 1898–1901 (2012).
46. Sananes, M., Tuel, A., Hutchings, G. & Volta, J. Characterization of different precursors and activated vanadium phosphate catalysts by ^{31}P NMR spin echo mapping. *J. Catal.* **148**, 395–398 (1994).
47. O'Dell, L. A., Rossini, A. J. & Schurko, R. W. Acquisition of ultra-wideline NMR spectra from quadrupolar nuclei by frequency stepped WURST–QCPMG. *Chem. Phys. Lett.* **468**, 330–335 (2009).
48. Pell, A. J. et al. Frequency-stepped acquisition in nuclear magnetic resonance spectroscopy under magic angle spinning. *J. Chem. Phys.* **138**, 114201 (2013).
49. Massiot, D. et al. ^{71}Ga and ^{69}Ga nuclear magnetic resonance study of β-Ga_2O_3: resolution of four-and six-fold coordinated Ga sites in static conditions. *Solid State Nucl. Magn. Reson.* **4**, 241–248 (1995).
50. McCloskey, B. D. et al. Solvents' critical role in nonaqueous lithium–oxygen battery electrochemistry. *J. Phys. Chem. Lett.* **2**, 1161–1166 (2011).

Acknowledgements

This work is supported by the Umicore Specialty Oxides and Chemicals and the Assistant Secretary of Energy Efficiency and Renewable Energy, Vehicle Technologies Office of the US Department of Energy (DOE) under contract no. DE-AC02-05CH11231 under the Advanced Battery Materials Research (BMR) Program. Recent characterization work was supported by the Assistant Secretary for Energy Efficiency and Renewable Energy, Vehicle Technologies Office, under the Applied Battery Materials Program, of the US DOE under contract no. DE-AC02-05CH11231. Work at the Advanced Light Source is supported by the Director, Office of Science, Office of Basic Energy Sciences, of the US DOE under contract no. DE-AC02-05CH11231. Research conducted at the Nanoscale Ordered Materials Diffractometer Beamline at Oak Ridge National Laboratory's Spallation Neutron Source is sponsored by the Scientific User Facilities Division, Office of Basic Sciences of the US DOE. Work at the Molecular Foundry at Lawrence Berkeley National Laboratory is supported by the Office of Science, Office of Basic Energy Sciences of the US DOE under contract no. DE-AC02-05CH11231. This research used resources of the Advanced Photon Source, an Office of Science User Facility operated for the US DOE Office of Science by Argonne National Laboratory, and is supported by the US DOE under contract no. DE-AC02-06CH11357. The NMR experimental work reported here made use of the shared facilities of the UCSB MRSEC (NSF DMR 1720256), a member of the Material Research Facilities Network. H.J. acknowledges support from the Assistant Secretary of Energy Efficiency and Renewable Energy, Vehicle Technologies Office of the US DOE, under contract no. DE-AC02-05CH11231. J.K.P. also acknowledges support from the NSF Graduate Research Fellowship under contract no. DGE-1106400.

Author contributions

H.J. and G.C. planned the project. G.C. supervised all aspects of the research. H.J. designed the proposed compounds. H.J. and Z.C. synthesized and electrochemically tested the compounds with help from H.K. J.W. performed the mRIXS measurements and analysed the data with input from W.Y. J.L. performed the neutron diffraction measurements and analysed the neutron and synchrotron diffraction data. D.-H.K. acquired and analysed the transmission electron microscopy, electron diffraction and EDS data. H.K. collected the operando XANES data with help from M.B. and Z.C. A.U. performed computational percolation analysis. J.K.P. acquired and analysed the differential electrochemical mass spectrometer data with input from B.D.M. E.F. acquired and analysed the NMR data with input from R.J.C. Y.T. collected SEM and synchrotron diffraction data. The manuscript was written by H.J. and G.C. and revised by A.U., J.W. and J.L. with the help from other authors.

Competing interests

The authors declare no competing interests.

Additional information

Supplementary information is available for this paper at https://doi.org/10.1038/s41560-020-0573-1.

Correspondence and requests for materials should be addressed to G.C.

Reprints and permissions information is available at www.nature.com/reprints.